APPLIED PHYSICS

Role of damping in spin Seebeck effect in yttrium iron garnet thin films

Houchen Chang,[1]* P. A. Praveen Janantha,[1]* Jinjun Ding,[1] Tao Liu,[1] Kevin Cline,[1] Joseph N. Gelfand,[1] Wei Li,[2] Mario C. Marconi,[2] Mingzhong Wu[1]†

The role of damping in the spin Seebeck effect (SSE) was studied experimentally for the first time. The experiments used $Y_3Fe_5O_{12}$ (YIG)/Pt bilayered structures where the YIG films exhibit very similar structural and static magnetic properties but very different damping. The data show that a decrease in the damping gives rise to an increase in the SSE coefficient, which is qualitatively consistent with some of the theoretical models. This response also shows quasi-linear behavior, which was not predicted explicitly by previous studies. The data also indicate that the SSE coefficient shows no notable correlations with the enhanced damping due to spin pumping, which can be understood in the frame of two existing models.

INTRODUCTION

The spin Seebeck effect (SSE) refers to the generation of a spin voltage in a ferromagnet (FM) due to a temperature gradient. This spin voltage can produce a pure spin current into a normal metal (NM) that is in contact with the FM. The SSE was first discovered in ferromagnetic metals (*1*–*3*), but not long after was also observed in magnetic insulators (*4*–*9*) and semiconductors (*10*, *11*). The experiments usually use an FM/NM bilayered heterostructure with the magnetization in the FM layer saturated in-plane and often take a longitudinal configuration in which a temperature gradient is established along the thickness direction of the FM/NM structure.

Various theoretical models have been proposed to interpret the SSE (*3*–*5*, *11*–*16*), although a complete understanding of the effect has not been realized yet. Among the early models, the one attracting slightly more interest is the so-called magnon-driven SSE model proposed by Xiao *et al.* (*12*). More recent models include those proposed in previous works (*13*–*16*). Although proposed separately, these recent models all involve magnon flows across the FM thickness and emphasize the bulk origin of the SSE. The bulk origin has been supported by SSE experiments using FM films of different thicknesses (*14*, *16*). The four SSE models mentioned above all engage the magnetic damping in the FM film as a critical ingredient of the SSE, although in very different ways, as summarized below.

The magnon-driven SSE model was developed on the basis of the stochastic Gilbert equation (*12*). The essence of this model is that the magnon subsystem in an FM can become thermalized internally before it equilibrates with the phonon subsystem. As a result, the spatial distribution of the magnon temperature T_m in the FM deviates from that of the phonon temperature T_p, although the average of T_m may be the same as that of T_p. This temperature distribution difference can further result in a difference between T_m in the FM and the electron temperature T_e in a neighboring NM at the interface and a corresponding pure spin current in the NM. This model yields an analytical expression for the spin current pumped from the FM to the NM. The expression involves the damping constant α in a rather complicated manner, but the general trend is that the spin current increases monotonically as α decreases.

In the study of Hoffman *et al.* (*13*), on the other hand, the origin of the SSE was analyzed using the stochastic Landau-Lifshitz theory. According to the model of Hoffman *et al.* (*13*), the magnons in the FM film establish a nonequilibrium steady state by coupling with phonons in the FM via bulk damping and with electrons in the neighboring NM via interfacial spin pumping. The analysis identified several characteristic length scales that governed the SSE strength, and for all of those scales, the SSE coefficient depends on α, although in different manners. In the case of a $Y_3Fe_5O_{12}$ (YIG) film thinner than 100 nm, the model suggests that the SSE coefficient is proportional to α, which is opposite to the abovementioned expectation of the model of Xiao *et al.* (*12*).

In contrast to Xiao *et al.* (*12*) and Hoffman *et al.* (*13*), in the study of Rezende *et al.* (*14*), the SSE phenomenon was studied through microscopic calculations using the Boltzmann equation of the magnons. In the model of Rezende *et al.* (*14*), the temperature gradient leads to the generation of the magnons in the bulk of the FM, and the magnon spin current into the NM is needed to ensure the continuity of the spin flow at the FM/NM interface. Different from the models of Xiao *et al.* (*12*) and Hoffman *et al.* (*13*), this model assumes that the magnon and phonon systems in the FM share the same temperature, as demonstrated in a slightly earlier experimental study (*17*). As in the study of Xiao *et al.* (*12*), in the study of Rezende *et al.* (*14*), the analytical expression for the spin current also involves α in a very complicated manner, but the main point of the model is that the spin current into the NM increases with a decrease in the magnon relaxation rate, whereas the latter increases with an increase in α.

Last, in the studies of Ritzmann *et al.* (*15*) and Kehlberger *et al.* (*16*), the SSE was examined by numerical simulations that took into account the linear dependence of the SSE strength on T_m-T_p in the FM near the interface (*12*) and considered the decay of T_m-T_p with a certain characteristic length scale from the interface into the bulk of the FM. The simulations show that, in the presence of a spatial temperature step in the FM, a magnon flow can arise from the hot side to the cold side, and the length of the magnon propagation is inversely proportional to α. Although no explicit analytical expression for the dependence of the spin current or the SSE coefficient on α was given, the simulation results revealed an increase in the SSE strength with a decrease in α.

Despite the above-discussed theoretical aspects, however, there have been no experiments on the actual effects of the damping on the SSE so

[1]Department of Physics, Colorado State University, Fort Collins, CO 80523, USA. [2]Engineering Research Center for Extreme Ultraviolet Science and Technology and Department of Electrical and Computer Engineering, Colorado State University, Fort Collins, CO 80523, USA.
*These authors contributed equally to this work.
†Corresponding author. Email: mwu@colostate.edu

far, to the best of our knowledge. There was an experimental investigation on the SSE that used a large number of diverse garnet ferrites exhibiting different damping properties (*18*). However, those materials did not allow for the study of the roles of α in the SSE because they had significantly different static magnetic properties.

This study reports on the role of the damping on the SSE in YIG thin films. The experiments used YIG films grown on $Gd_3Ga_5O_{12}$ (GGG) substrates by sputtering (*19*, *20*). The films showed very similar structural and static magnetic properties but rather different α values, resulting from careful control of fabrication conditions. To probe the strength of the SSE, a Pt capping layer was grown on each YIG sample. During the SSE measurements, the temperature at the Pt side of the sample was kept constant, whereas that at the GGG side was varied to realize a temperature difference (ΔT) across the sample thickness. Upon the presence of ΔT, the SSE takes place and produces a pure spin current in the Pt layer. Via the inverse spin Hall effect (ISHE) (*21*–*23*), the spin current then produces an electric voltage (V) across one of the lateral dimensions of the Pt layer. The SSE-produced voltage V was measured as a function of ΔT. The data show that the slope of the V versus ΔT response increases with a decrease in α. This indicates that the smaller the damping is, the stronger the SSE is. This result is qualitatively consistent with the theoretical models in previous works (*12*, *14*–*16*). Furthermore, the SSE coefficient versus α response shows almost linear behavior, which was not predicted explicitly in previous works (*12*, *14*–*16*). The experiments also indicate that the SSE strength shows no notable correlations with the enhanced damping due to spin pumping at the YIG/Pt interface. This can be understood in the frame of the models described by Xiao *et al.* (*12*) and Kehlberger *et al.* (*16*).

RESULTS AND DISCUSSIONS

Properties of YIG and YIG/Pt samples

The main properties of the YIG and YIG/Pt thin-film samples are given in Fig. 1 and Table 1. Complete descriptions about these samples are provided in the Supplementary Materials. The YIG films were grown on 0.5-mm-thick (111) GGG substrates by radio frequency (RF) sputtering. The general details on the growth, structure, and static magnetic properties of the films are provided in previous works (*19*, *20*, *24*). The Pt capping layers were grown by dc sputtering at room temperature and were all 5 nm thick.

Figure 1 presents the ferromagnetic resonance (FMR) data. Figure 1 (A and B) presents the FMR field H_{FMR} and peak-to-peak FMR linewidth ΔH, respectively, as a function of frequency f for bare YIG film sample #5 for two different field configurations. The symbols show the data. The lines in Fig. 1A show fits to the Kittel equations

$$f = |\gamma|\sqrt{H(H + 4\pi M_{\text{eff}})} \quad (1)$$

and

$$f = |\gamma|(H - 4\pi M_{\text{eff}}) \quad (2)$$

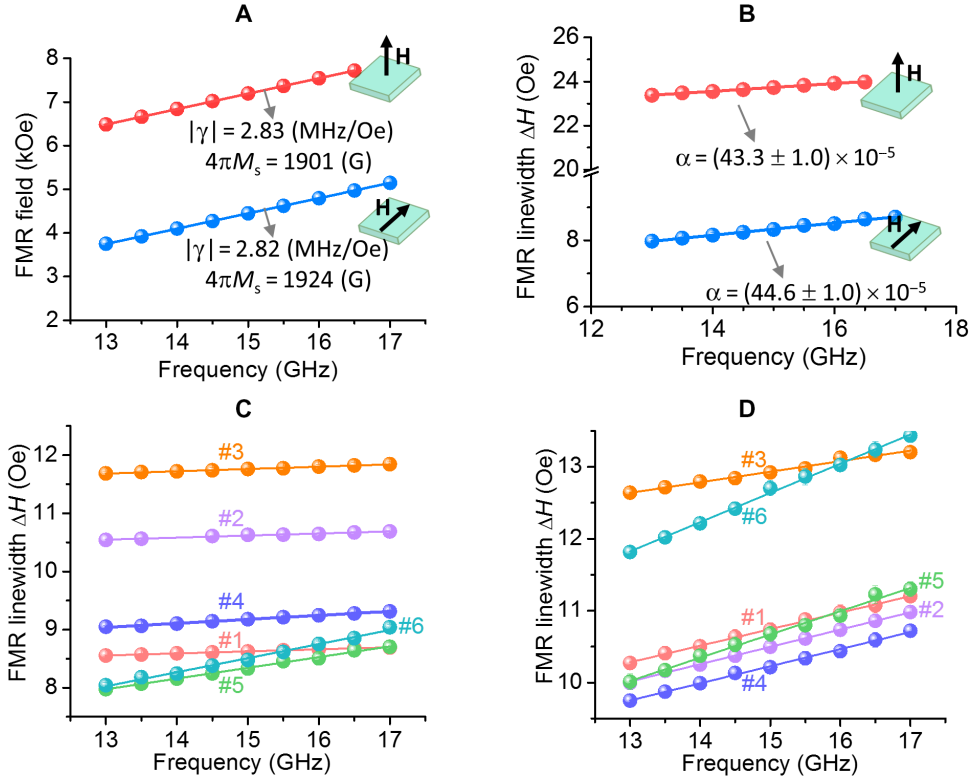

Fig. 1. FMR properties of bare YIG thin-film samples and YIG/Pt bilayered samples. (**A** and **B**) Graphs showing the FMR field (A) and linewidth (B) as a function of frequency for two different field (*H*) configurations for bare YIG film sample #5. The dots show the data, and the lines show the fits. The fitting-yielded parameters are also given. (**C** and **D**) Graphs presenting the FMR linewidth data (dots) and fits (lines) for six bare YIG film samples (C) and the data and fits for the corresponding YIG films after the growth of a 5-nm-thick Pt capping layer (D).

where $|\gamma|$ is the absolute gyromagnetic ratio, H is the external magnetic field, and $4\pi M_{eff}$ is the effective saturation induction. Equations 1 and 2 are for the field-in-plane and field-out-of-plane configurations, respectively. The $|\gamma|$ and $4\pi M_{eff}$ values indicated in Fig. 1A were obtained from the fitting. The lines in Fig. 1B show fits to

$$\Delta H = \frac{2\alpha}{\sqrt{3}|\gamma|} f + \Delta H_0 \quad (3)$$

where ΔH_0 accounts for inhomogeneous linewidth broadening and does not represent a loss. The fitting-produced α values are also given in Fig. 1B. From Fig. 1 (A and B), one can see that the $|\gamma|$, $4\pi M_{eff}$, and α values obtained for the field-in-plane configuration are almost the same as those obtained for the out-of-plane configuration. Moreover, this is true for other samples, although not presented. This consistency indicates two results. First, it clearly shows the reliability of the FMR results obtained with either field configuration. Second, the consistency of the α values for the two field configurations suggests that the contribution of two-magnon scattering to α is negligible in the YIG films. In the case that two-magnon scattering occurs, one would expect the α values measured with in-plane fields to be notably larger than those measured with out-of-plane fields (*25*, *26*). It should be noted that the $4\pi M_{eff}$ values presented here may include a perpendicular anisotropy field contribution, but this contribution, if present, is expected to be small, considering the facts that the YIG films have very weak magnetocrystalline anisotropy (*27*, *28*) and minimal strain-induced anisotropy due to almost perfect lattice matching with the GGG substrates and the high-temperature annealing process. In addition, none of the previous works on YIG thin films reported the presence of notable perpendicular anisotropy in the films (*19*, *20*, *29*–*31*).

Figure 1C presents the ΔH versus f data for six bare YIG film samples. As in Fig. 1B, the symbols show the ΔH data and the lines show the fits to Eq. 3. One can see that all of the six sets of data can be fitted very well. The fitting-yielded damping values, termed as α_{YIG}, are listed in Table 1. Figure 1D shows the ΔH versus f data, in the same format as in Fig. 1C, for the YIG samples after the deposition of a Pt capping layer. One can see that the growth of a Pt layer not only enhances ΔH but also results in a notable increase in the slopes. As in Fig. 1C, all of the six sets of data in Fig. 1D can be fitted very well. The fitting-yielded damping values, termed as $\alpha_{YIG/Pt}$, are also given in Table 1. Note that the data in Fig. 1 (C and D) were measured with in-plane fields.

Table 1 lists the fitting-yielded $4\pi M_{eff}$, α_{YIG}, and $\alpha_{YIG/Pt}$ values as well as the YIG film thickness (D) values of the six samples. It is evident from Table 1 that the six YIG films have very similar thicknesses and comparable $4\pi M_{eff}$ values, but their α_{YIG} values differ by a factor of about 7. Since magnon-electron scattering does not occur in insulators, two-magnon scattering is negligible, as discussed above, three-magnon scattering is prohibited because the FMR frequency is relatively high, and four-magnon scattering is relatively weak because of low microwave power (3 dBm) in the FMR measurements, one can conclude that the α_{YIG} values listed in Table 1 denote the intrinsic magnetic damping in the YIG films and result mainly from magnon-phonon scattering. Note that the magnon-phonon scattering refers to a relaxation process in which a magnon is annihilated, some phonons are created, and perhaps other phonons are annihilated (*27*). Via this scattering, the energy of the magnons dissipates into the lattice of the material. Considering the facts that the six YIG films exhibit very similar structural and static magnetic properties but show very different damping, it can be concluded that the films constitute a good system for exploring the role of damping in the SSE. Detailed justifications for this conclusion are provided in section S4. It should be noted that the average of the six $4\pi M_{eff}$ values given in Table 1 is 1866 G, and the corresponding standard deviation is 70 G, indicating that the $4\pi M_{eff}$ values are comparable. This fact is important for the determination of the roles of the damping in the SSE because the SSE strength varies with $4\pi M_{eff}$, as demonstrated by previous experimental studies (*18*).

Table 1. Properties of six YIG thin-film samples before and after the growth of a 5-nm-thick Pt capping layer.

Sample	#1	#2	#3	#4	#5	#6
D (nm)	23.4	23.4	23.4	23.4	19.7	22.3
$4\pi M_{eff}$ (G)	1820	1956	1757	1827	1924	1913
α_{YIG} ($\times 10^{-5}$)	8.5±0.2	8.7±0.5	9.4±0.3	16.5±0.3	45±1	59±2
$\alpha_{YIG/Pt}$ ($\times 10^{-5}$)	55.8±0.8	58.4±0.8	35±1	58±1	77±2	99±2
α_{sp} ($\times 10^{-5}$) ($= \alpha_{YIG/Pt} - \alpha_{YIG}$)	47.3	49.7	25.6	41.5	32	40

After the growth of a Pt capping layer, however, the damping in the YIG also contains a contribution due to spin pumping from the YIG to the Pt. As a result, the damping consists of two components, namely, $\alpha_{YIG/Pt} = \alpha_{YIG} + \alpha_{sp}$, where α_{YIG} describes the contribution from the relaxation in the bulk of the YIG and α_{sp} describes the interfacial spin pumping contribution. It is fortunate that these two components, α_{YIG} and α_{sp}, can be separated, as listed in rows 4 and 6 in Table 1, facilitating the examination of the effects of each component on the SSE, as discussed shortly. Three points should be made about α_{sp}. First, α_{sp} can be considered to be a result of the coupling between the magnons in the YIG and the electrons in the Pt; it should also contain a contribution from the coupling of the magnons in the YIG to the phonons in the Pt, but this contribution is expected to be much weaker than that of the magnon-electron coupling at the interface. Second, in addition to α_{sp}, the growth of the Pt capping layer might also lead to an enhancement in the surface imperfection-associated damping in the YIG film. However, this damping should be much smaller than α_{sp}, as shown by previous experimental studies on the damping in YIG/Cu and YIG/Cu/Pt layered samples (*32*). Finally, α_{sp} changes from sample to sample, ranging from 25.6×10^{-5} for sample #3 to 49.7×10^{-5} for sample #2, and this variation is likely due to the YIG surface quality (such as the texture; see fig. S3) and associated difference in the quality of the YIG/Pt interface. However, the range of the α_{sp} variation is significantly narrower than that of the α_{YIG} variation.

SSE measurements

Turn now to the SSE experiments on the YIG/Pt samples. Figure 2A shows a schematic of the experimental setup. During the SSE measurement, an external field of about 930 Oe was applied in-plane and perpendicular to the length of the YIG/Pt strip. The temperature at the Pt side of the YIG/Pt sample, T_{Pt}, was kept constant, whereas the temperature at the GGG side of the sample, T_{GGG}, was varied. When the difference $\Delta T = T_{GGG} - T_{Pt}$ is nonzero, the SSE occurs in the YIG and produces a pure spin current flowing into the Pt. The spin current then yields a measurable voltage V across the length of the Pt strip via the ISHE (*21*–*23*). Note that the purpose of keeping T_{Pt} constant

is to minimize the change of the average temperature of the YIG and thereby to avoid the effects due to the change of the absolute temperature.

Figure 2 (B to D) presents SSE data obtained with YIG/Pt sample #1. Figure 2B presents the T_{Pt} and T_{GGG} data, whereas Fig. 2C presents ΔT (left axis) and the corresponding V data (right axis). One can see that, during the measurements, T_{Pt} was kept constant at 15.5°C, T_{GGG} was varied over a range of about 15° to 33°C, and V changed in almost the same manner as ΔT. These results indicate that the voltage signal is associated with the temperature gradient in the YIG, rather than the absolute temperature of the YIG or the Pt. Note that one can consider that the average temperature in the YIG was almost constant just as T_{Pt}, based on the fact that the GGG substrate (0.5 mm) is considerably thicker than the YIG film (≈20 nm). Figure 2D plots V as a function of ΔT using the data in Fig. 1C. The red coarse line consists of the experimental data points, and the blue thin line shows a fit. One can see that the V versus ΔT response is almost perfectly linear. This linear behavior is expected by all the four SSE models described in the Introduction (*12*–*14*, *16*).

Several additional notes should be made regarding the data shown in Fig. 2. First, it should be mentioned that reversing the magnetic field direction resulted in a flip in the voltage sign, as shown in fig. S5. This is the same as previously reported (*6*, *9*). It is because the direction of the magnetization in the YIG film dictates the polarization direction of the SSE-produced spin current in the Pt layer. Second, the data in Fig. 2D do not show any hysteresis or loop behavior in response to the change of ΔT from 0°C to about 17°C first and then back to 0°C. This indicates that the GGG side of the sample reached a quasi-equilibrium during the SSE measurements. Finally, the measured SSE voltage might contain a small contribution from the anomalous Nernst effect in the Pt layer. However, such a contribution is expected to be negligible in comparison with the SSE signal, as demonstrated by a very recent experimental study (*33*).

Roles of damping on the SSE

Figure 3 presents the key results of this work. Figure 3A presents the SSE-produced V as a function of ΔT for six YIG/Pt samples, as indicated. Figure 3B presents the linear fits to the data in Fig. 3A. In Fig. 3B, the y axis intercepts are all removed for a better presentation. Those intercepts are independent of ΔT and are therefore not associated with the SSE. They might result from the conventional Seebeck effect–produced voltage in response to a possible temperature gradient along the Pt length and small voltage offsets in the voltmeter. One can significantly reduce those voltage intercepts (see fig. S5) by carefully arranging the experimental setup. If one takes D as the sample thickness and L as the distance between the two electrodes (see Fig. 2A) and defines (*34*)

$$\xi_{SSE} = \frac{(V/L)}{(\Delta T/D)} = \frac{V}{\Delta T}\frac{D}{L} \quad (4)$$

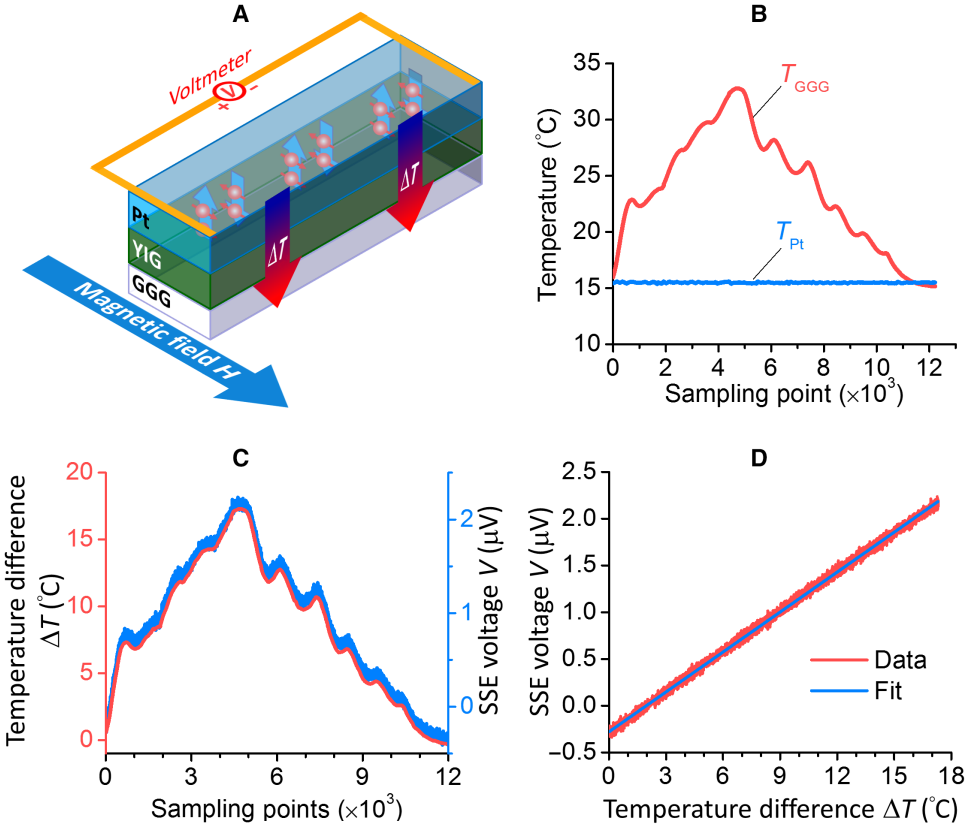

Fig. 2. SSE measurements. (**A**) Graph showing a schematic of the experimental setup. (**B** to **D**) Graphs showing the data obtained with YIG/Pt sample #1. (B) Temperatures on the Pt and GGG sides of the sample, T_{Pt} and T_{GGG}. (C) ΔT (= T_{GGG} − T_{Pt}) and the corresponding voltage signal V. The horizontal axes in (B) and (C) show sampling points, and 1000 points correspond to a period of 4 min. (D) The V versus ΔT response plotted using the data in (C). The thin blue line in (D) shows a linear fit.

as the geometry-free SSE coefficient, then one can use the slope of the V versus ΔT lines in Fig. 3B to determine the ξ_{SSE} values for different samples and thereby examine how ξ_{SSE} varies with the damping by plotting ξ_{SSE} as a function of α_{YIG}, α_{sp}, or $\alpha_{YIG} + \alpha_{sp}$. These plots are presented in Fig. 3 (C to E).

It is evident from the data in Fig. 3C that ξ_{SSE} increases with a decrease in α_{YIG}, indicating that the SSE is stronger if the damping is weaker. This result is qualitatively consistent with the theoretical models proposed by Xiao *et al.* (*12*) and Rezende *et al.* (*14*) and the simulation results presented by Ritzmann *et al.* (*15*) and Kehlberger *et al.* (*16*). The underlying physics is that the damping in the YIG films originates mainly from magnon-phonon scattering, as discussed above; the weaker the magnons are coupled to the phonons, the more the magnon temperature T_m deviates from the phonon temperature T_p at the YIG/Pt interface, according to the model proposed by Xiao *et al.* (*12*). Note that a previous work has demonstrated a good agreement between the simulations using this model and the experiments using YIG/Pt heterostructures (*35*). In the terminology described in previous works (*14*–*16*), the underlying physics is that the weaker the damping is, the more the magnons propagate from the bulk to the interface and contribute to the SSE signal. Furthermore, the data in Fig. 3C also indicate that the ξ_{SSE} versus α_{YIG} response shows quasi-linear behavior for the given damping range, as suggested by the red dashed line. Understanding of this quasi-linear response calls for new theoretical studies.

In a stark contrast, the data in Fig. 3D do not show any obvious correlations between ξ_{SSE} and α_{sp}. This can be understood in the frame of the SSE models described by Xiao *et al.* (*12*) and Kehlberger *et al.* (*16*). Specifically, α_{sp} plays two roles in the process, in which the SSE in the YIG produces spin currents in the Pt. On the one hand, a larger α_{sp} value indicates a more efficient spin transfer at the YIG/Pt interface (*36*), and one should therefore expect larger spin currents in the Pt in samples with larger α_{sp}. On the other hand, the spin transfer at the YIG/Pt interface at the same time causes a decrease in the difference between T_m in the YIG and T_e in the Pt near the interface, resulting in a weaker SSE. One can see that these two roles are opposite, and as a result, ξ_{SSE} does not show an explicit dependence on α_{sp}. Note that the blue dashed line in Fig. 3D indicates the average ξ_{SSE}.

Considering that some of the previous theoretical analyses involved the total damping in the FM (*12*, *13*), in Fig. 3E, ξ_{SSE} is plotted as a function of $\alpha_{YIG} + \alpha_{sp}$. One can see that the overall trend is ξ_{SSE} increases with a decrease in $\alpha_{YIG} + \alpha_{sp}$. This trend results from the fact that ξ_{SSE} clearly increases with decreasing α_{YIG} but shows no explicit correlations with α_{sp}, as discussed above.

CONCLUSIONS

In summary, the effects of the intrinsic damping in the YIG bulk (α_{YIG}) and the enhanced damping due to interfacial spin pumping (α_{sp}) on the SSE in the YIG/Pt bilayered structures have been studied experimentally. The experimental data show that the smaller the damping α_{YIG} is, the stronger the SSE is. This observation is consistent with some of the existing theoretical models (*12*, *14*–*16*). The SSE coefficient versus α_{YIG} response is almost linear. This quasi-linear behavior was not predicted explicitly by previous models. The data also show no explicit correlations between the SSE strength and α_{sp}, which can be interpreted using the terminology of two existing models (*12*, *16*). One can expect similar results in other magnetic insulator/NM heterostructures. However, the results might be different in ferromagnetic metal/NM heterostructures

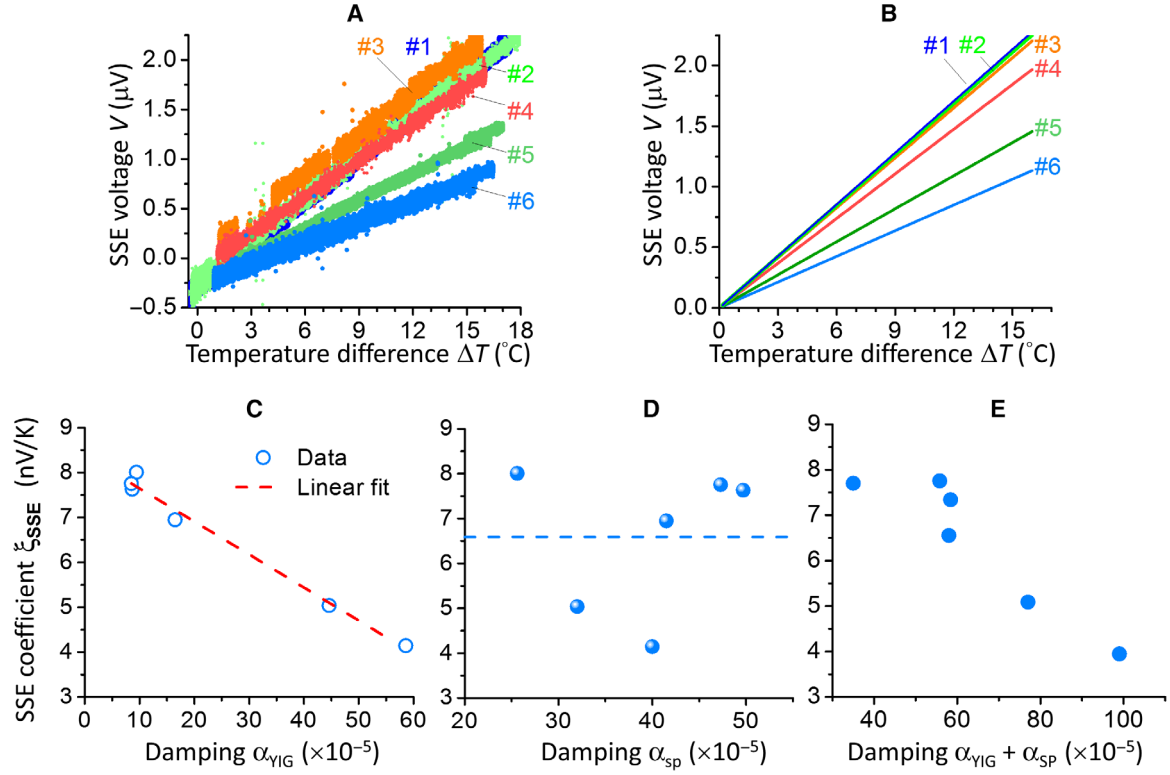

Fig. 3. Effects of damping in the SSE. (**A**) Graph showing the SSE-produced voltage as a function of ΔT (= $T_{GGG} - T_{Pt}$) measured on six different YIG/Pt samples. (**B**) Graph showing the linear fits to the data in (A). (**C** to **E**) Graphs showing the SSE coefficient, which is defined by Eq. 4, as a function of α_{YIG} (C), α_{sp} (D), and $\alpha_{YIG} + \alpha_{sp}$ (E).

because of the facts that (i) in ferromagnetic metals, magnon-electron scattering plays critical roles in the intrinsic damping (*27*, *37*, *38*) and (ii) the spin transfer at a ferromagnetic metal/NM interface is significantly more efficient than that at a magnetic insulator/NM interface (*39*, *40*).

MATERIALS AND METHODS

The YIG thin films were first grown on 0.5-mm-thick, (111)-oriented GGG substrates by RF magnetron sputtering at room temperature and were then annealed in situ at high temperature in oxygen. The sputtered YIG thin films were 10-mm by 10-mm squares. They were then cut into smaller pieces. One of these YIG pieces (about 3 mm by 10 mm) was used for the deposition of a Pt capping layer, and the resultant YIG/Pt strip sample was then used for the SSE measurements. The other YIG pieces (about 3 mm by 3 mm) were used for characterizations, which included x-ray diffraction, x-ray rocking curve, x-ray photoelectron spectroscopy, atomic force microscopy, and FMR measurements. The Pt capping layers were grown by dc magnetron sputtering at room temperature. During the SSE experiments on the YIG/Pt strip samples, the temperature on the Pt side of the YIG/Pt sample, T_{Pt}, was kept constant. This was realized by placing a Peltier device on the Pt side of the sample, inserting a thermal couple in between the Peltier device and the sample to measure T_{Pt}, and using a computer to take the feedback from the couple to control the Peltier device. A second Peltier device was placed on the GGG side of the sample to vary its temperature, T_{GGG}, which was probed by another thermal couple inserted in between the Peltier device and the GGG substrate. When the temperature difference $\Delta T = T_{GGG} - T_{Pt}$ was nonzero, the SSE occurred in the YIG film and produced a pure spin current flowing across the Pt thickness, which was detected by a Keithley 2182A nanovoltmeter.

SUPPLEMENTARY MATERIALS

Supplementary material for this article is available at http://advances.sciencemag.org/cgi/content/full/3/4/e1601614/DC1

section S1. Sample fabrication
section S2. Crystalline and structural properties of samples
section S3. Magnetic properties of samples
section S4. Summary of sample properties
section S5. SSE experiments
table S1. Major control parameters for YIG thin-film fabrication.
table S2. Surface root-mean-square roughness (nanometers) of bare YIG and YIG/Pt film samples.
table S3. Properties of six YIG thin-film samples before and after the growth of a 5-nm-thick Pt capping layer.
fig. S1. X-ray photoelectron spectroscopy data for five YIG thin-film samples.
fig. S2. X-ray photoelectron spectroscopy data for five YIG thin-film samples.
fig. S3. Atomic force microscopy surface images of five YIG thin-films samples.
fig. S4. FMR properties of bare YIG thin-film samples and YIG/Pt bilayered samples.
fig. S5. Effects of the magnetic field direction on the SSE.
References (*41*–*48*)

REFERENCES AND NOTES

1. K. Uchida, S. Takahashi, K. Harii, J. Ieda, W. Koshibae, K. Ando, S. Maekawa, E. Saitoh, Observation of the spin Seebeck effect. *Nature* **455**, 778–781 (2008).
2. K. Uchida, T. Ota, K. Harii, S. Takahashi, S. Maekawa, Y. Fujikawa, E. Saitoh, Spin-Seebeck effects in NiFe/Pt films. *Solid State Commun.* **150**, 524–528 (2010).
3. K. Uchida, H. Adachi, T. An, T. Ota, M. Toda, B. Hillebrands, S. Maekawa, E. Saitoh, Long-range spin Seebeck effect and acoustic spin pumping. *Nat. Mater.* **10**, 737–741 (2011).
4. K. Uchida, J. Xiao, H. Adachi, J. Ohe, S. Takahashi, J. Ieda, T. Ota, Y. Kajiwara, H. Umezawa, H. Kawai, G. E. W. Bauer, S. Maekawa, E. Saitoh, Spin Seebeck insulator. *Nat. Mater.* **9**, 894–897 (2010).
5. H. Adachi, K.-i. Uchida, E. Saitoh, J.-i. Ohe, S. Takahashi, S. Maekawa, Gigantic enhancement of spin Seebeck effect by phonon drag. *Appl. Phys. Lett.* **97**, 252506 (2010).
6. K.-i. Uchida, T. Nonaka, T. Ota, E. Saitoh, Longitudinal spin-Seebeck effect in sintered polycrystalline (Mn,Zn)Fe_2O_4. *Appl. Phys. Lett.* **97**, 262504 (2011).
7. E. Padrón-Hernández, A. Azevedo, S. M. Rezende, Amplification of spin waves by thermal spin-transfer torque. *Phys. Rev. Lett.* **107**, 197203 (2011).
8. M. B. Jungfleisch, T. An, K. Ando, Y. Kajiwara, K. Uchida, V. I. Vasyuchka, A. V. Chumak, A. A. Serga, E. Saitoh, B. Hillebrands, Heat-induced damping modification in yttrium iron garnet/platinum hetero-structures. *Appl. Phys. Lett.* **102**, 062417 (2013).
9. D. Qu, S. Y. Huang, J. Hu, R. Wu, and C. L. Chien, Intrinsic spin Seebeck effect in Au/YIG. *Phys. Rev. Lett.* **110**, 067206 (2013).
10. C. M. Jaworski, J. Yang, S. Mack, D. D. Awschalom, J. P. Heremans, R. C. Myers, Observation of the spin-Seebeck effect in a ferromagnetic semiconductor. *Nat. Mater.* **9**, 898–903 (2010).
11. C. M. Jaworski, J. Yang, S. Mack, D. D. Awschalom, R. C. Myers, J. P. Heremans, Spin-seebeck effect: A phonon driven spin distribution. *Phys. Rev. Lett.* **106**, 186601 (2011).
12. J. Xiao, G. E. W. Bauer, K.-i. Uchida, E. Saitoh, S. Maekawa, Theory of magnon-driven spin Seebeck effect. *Phys. Rev. B* **81**, 214418 (2010).
13. S. Hoffman, K. Sato, Y. Tserkovnyak, Landau-Lifshitz theory of the longitudinal spin Seebeck effect. *Phys. Rev. B* **88**, 064408 (2013).
14. S. M. Rezende, R. L. Rodríguez-Suárez, R. O. Cunha, A. R. Rodrigues, F. L. A. Machado, G. A. Fonseca Guerra, J. C. Lopez Ortiz, A. Azevedo, Magnon spin-current theory for the longitudinal spin-Seebeck effect. *Phys. Rev. B* **89**, 014416 (2014).
15. U. Ritzmann, D. Hinzke, U. Nowak, Propagation of thermally induced magnonic spin currents. *Phys. Rev. B* **89**, 024409 (2014).
16. A. Kehlberger, U. Ritzmann, D. Hinkzke, E.-J. Guo, J. Cramer, G. Jakob, M. C. Onbasli, D. Kim, C. A. Ross, M. B. Jungfleisch, B. Hillebrands, U. Nowak, M. Kläui, Length scale of the spin Seebeck effect. *Phys. Rev. Lett.* **115**, 096602 (2015).
17. M. Agrawal, V. I. Vasyuchka, A. A. Serga, A. D. Karenowska, G. A. Melkov, and B. Hillebrands, Direct measurement of magnon temperature: New insight into magnon-phonon coupling in magnetic insulators. *Phys. Rev. Lett.* **111**, 107204 (2013).
18. K. Uchida, T. Nonak, T. Kikkawa, Y. Kajiwara, E. Saitoh, Longitudinal spin Seebeck effect in various garnet ferrites. *Phys. Rev. B* **87**, 104412 (2013).
19. T. Liu, H. Chang, V. Vlaminck, Y. Sun, M. Kabatek, A. Hoffmann, L. Deng, M. Wu, Ferromagnetic resonance of sputtered yttrium iron garnet nanometer films. *J. Appl. Phys.* **115**, 17A501 (2014).
20. H. Chang, P. Li, W. Zhang, T. Liu, A. Hoffmann, L. Deng, M. Wu, Nanometer-thick yttrium iron garnet films with extremely low damping. *IEEE Magn. Lett.* **5**, 6700104 (2014).
21. J. E. Hirsch, Spin hall effect. *Phys. Rev. Lett.* **83**, 1834–1837 (1999).
22. S. O. Valenzuela, M. Tinkham, Direct electronic measurement of the spin Hall effect. *Nature* **442**, 176–179 (2006).
23. A. Hoffmann, Spin hall effects in metals. *IEEE Trans. Magn.* **49**, 5172–5193 (2013).
24. E. Jakubisova-Liskova, S. Visnovsky, H. Chang, M. Wu, Optical spectroscopy of sputtered nanometer-thick yttrium iron garnet films. *J. Appl. Phys.* **117**, 17B702 (2015).
25. R. D. McMichael, P. Krivosik, Classical model of extrinsic ferromagnetic resonance linewidth in ultrathin films. *IEEE Trans. Magn.* **40**, 2–11 (2004).
26. P. Krivosik, N. Mo, S. Kalarickal, C. E. Patton, Hamiltonian formalism for two magnon scattering microwave relaxation: Theory and applications. *J. Appl. Phys.* **101**, 083901 (2007).
27. M. Sparks, *Ferromagnetic-Relaxation Theory* (McGraw-Hill, 1964).
28. M. Wu, A. Hoffmann, *Recent Advances in Magnetic Insulators - From Spintronics to Microwave Applications* (Academic Press, 2013), 432 pp.
29. Y. Sun, Y.-Y. Song, H. Chang, M. Kabatek, M. Jantz, W. Schneider, M. Wu, H. Schultheiss, A. Hoffmann, Growth and ferromagnetic resonance properties of nanometer-thick yttrium iron garnet films. *Appl. Phys. Lett.* **101**, 152405 (2012).
30. O. d'Allivy Kelly, A. Anane, R. Bernard, J. Ben Youssef, C. Hahn, A.-H. Molpceres, C. Carrétéro, E. Jacquet, C. Deranlot, P. Bortolotti, R. Lebourgeois, J.-C. Mage, G. de Loubens, O. Klein, V. Cros, A. Fert, Inverse spin Hall effect in nanometer-thick yttrium iron garnet/Pt system. *Appl. Phys. Lett.* **103**, 082408 (2013).
31. C. Tang, M. Aldosary, Z. Jiang, H. Chang, B. Madon, K. Chan, M. Wu, J. E. Garay, J. Shi, Exquisite growth control and magnetic properties of yttrium iron garnet thin films. *Appl. Phys. Lett.* **108**, 102403 (2016).
32. Y. Sun, H. Chang, M. Kabatek, Y.-Y. Song, Z. Wang, M. Jantz, W. Schneider, M. Wu, E. Montoya, B. Kardasz, B. Heinrich, S. G. E. te Velthuis, H. Schultheiss, A. Hoffmann, Damping in yttrium iron garnet nanoscale films capped by platinum. *Phys. Rev. Lett.* **111**, 106601 (2013).
33. B. F. Miao, S. Y. Huang, D. Qu, C. L. Chien, Absence of anomalous Nernst effect in spin Seebeck effect of Pt/YIG. *AIP Adv.* **6**, 015018 (2016).

34. A. Sola, M. Kuepferling, V. Basso, M. Pasquale, T. Kikkawa, K. Uchida, E. Saitoh, Evaluation of thermal gradients in longitudinal spin Seebeck effect measurements. *J. Appl. Phys.* **117**, 17C510 (2015).
35. M. Schreier, A. Kamra, M. Weiler, J. Xiao, G. E. W. Bauer, R. Gross, S. T. B. Goennenwein, Magnon, phonon, and electron temperature profiles and the spin Seebeck effect in magnetic insulator/normal metal hybrid structures. *Phys. Rev. B* **88**, 094410 (2013).
36. B. Heinrich, C. Burrowes, E. Montoya, B. Kardasz, E. Girt, Y.-Y. Song, Y. Sun, M. Wu, Spin pumping at the magnetic insulator (YIG)/normal metal (Au) interfaces. *Phys. Rev. Lett.* **107**, 066604 (2011).
37. J. Kuneš, V. Kamberský, First-principles investigation of the damping of fast magnetization precession in ferromagnetic 3*d* metals. *Phys. Rev. B* **65**, 212411 (2002).
38. K. Gilmore, Y. U. Idzerda, M. D. Stiles, Identification of the dominant precession-damping mechanism in Fe, Co, and Ni by first-principles calculations. *Phys. Rev. Lett.* **99**, 027204 (2007).
39. R. Urban, G. Woltersdorf, B. Heinrich, Gilbert damping in single and multilayer ultrathin films: Role of interfaces in nonlocal spin dynamics. *Phys. Rev. Lett.* **87**, 217204 (2011).
40. Y. Tserkovnyak, A. Brataas, G. E. W. Bauer, Enhanced Gilbert damping in thin ferromagnetic films. *Phys. Rev. Lett.* **88**, 117601 (2002).
41. T. Yamashita, P. Hayes, Analysis of XPS spectra of Fe^{2+} and Fe^{3+} ions in oxide materials. *Appl. Surf. Sci.* **254**, 2441–2449 (2008).
42. Y. Zhang, J. Xie, L. Deng, L. Bi, Growth of phase pure yttrium iron garnet thin films on silicon: The effect of substrate and post deposition annealing temperatures. *IEEE Trans. Magn.* **51**, 2503604 (2015).
43. L. Lu, Z. Wang, G. Mead, C. Kaiser, Q. Leng, M. Wu, Damping in free layers of tunnel magneto-resistance readers. *Appl. Phys. Lett.* **105**, 012405 (2014).
44. E. Jakubisova-Liskova, S. Visnovsky, H. Chang, M. Wu, Interface effects in nanometer-thick yttrium iron garnet films studied by magneto-optical spectroscopy. *Appl. Phys. Lett.* **108**, 082403 (2016).
45. S. Takahashi, E. Saitoh, S. Maekawa, Spin current through a normal-metal/insulating-ferromagnet Junction. *J. Phys. Conf. Ser.* **200**, 062030 (2010).
46. J. S. Agustsson, U. B. Arnalds, A. S. Ingason, K. B. Gylfason, K. Johnsen, S. Olafsson, J. T. Gudmundsson, Electrical resistivity and morphology of ultra thin Pt films grown by dc magnetron sputtering on SiO_2. *J. Phys. Conf. Ser.* **100**, 082006 (2008).
47. B. M. Howe, S. Emori, H.-M. Jeon, T. M. Oxholm, J. G. Jones, K. Mahalingam, Y. Zhuang, N. X. Sun, G. J. Brown, Pseudomorphic yttrium iron garnet thin films with low damping and inhomogeneous linewidth broadening. *IEEE Magn. Lett.* **6**, 3500504 (2015).
48. D. D. Stancil, A. Prabhakar, *Spin Waves: Theory and Applications* (Springer, 2009).

Acknowledgments: We gratefully acknowledge the discussions with J. Xiao at the Fudan University. **Funding:** This work was primarily supported by the Spins and Heat in Nanoscale Electronic Systems, an Energy Frontier Research Center funded by the U.S. Department of Energy, Office of Science, Basic Energy Sciences under award SC0012670. In addition, the fabrication and characterization of all the YIG and YIG/Pt samples were supported by the NSF under award EFMA-1641989. The FMR and spin pumping measurements and the corresponding data analysis were supported by the Center for Spintronic Materials, Interfaces, and Novel Architectures, one of the Semiconductor Research Corporation STARnet Centers sponsored by the Microelectronics Advanced Research Corporation and the Defense Advanced Research Projects Agency, and the U.S. Army Research Office under award W911NF-14-1-0501. **Author contributions:** H.C., P.A.P.J., and M.W. conceived the idea and designed the experiments. H.C. and T.L. prepared the samples, and H.C., J.D., T.L., W.L., and M.C.M. characterized the samples. P.A.P.J. conducted the SSE measurements. H.C., K.C., and J.N.G. contributed to the SSE measurements. H.C. and P.A.P.J. carried out data analyses. M.W. supervised the study. H.C., P.A.P.J., and M.W. wrote the manuscript and the Supplementary Materials with help from all the other co-authors. **Competing interests:** The authors declare that they have no competing interests. **Data and materials availability:** All data needed to evaluate the conclusions in the paper are present in the paper and/or the Supplementary Materials. Additional data related to this paper may be requested from the authors.

Submitted 13 July 2016
Accepted 10 February 2017
Published 7 April 2017
10.1126/sciadv.1601614

Citation: H. Chang, P. A. Praveen Janantha, J. Ding, T. Liu, K. Cline, J. N. Gelfand, W. Li, M. C. Marconi, M. Wu, Role of damping in spin Seebeck effect in yttrium iron garnet thin films. *Sci. Adv.* **3**, e1601614 (2017).

Role of damping in spin Seebeck effect in yttrium iron garnet thin films

Houchen Chang, P. A. Praveen Janantha, Jinjun Ding, Tao Liu, Kevin Cline, Joseph N. Gelfand, Wei Li, Mario C. Marconi and Mingzhong Wu

Sci Adv **3** (4), e1601614.
DOI: 10.1126/sciadv.1601614